DRAFT VERSION MARCH 1, 2019
Typeset using LaTeX **twocolumn** style in AASTeX62

Close-in sub-Neptunes reveal the past rotation history of their host stars: atmospheric evolution of planets in the HD3167 and K2-32 planetary systems

D. Kubyshkina[1], P. E. Cubillos[1], L. Fossati[1], N. V. Erkaev[2,3], C. P. Johnstone[4], K. G. Kislyakova[4,1], H. Lammer[1], M. Lendl[1], P. Odert[5,1], and M. Güdel[4]

[1]*Space Research Institute, Austrian Academy of Sciences, Schmiedlstrasse 6, A-8042 Graz, Austria*
[2]*Institute of Computational Modeling of the Siberian Branch of the Russian Academy of Sciences, 660036 Krasnoyarsk, Russian Federation*
[3]*Siberian Federal University, 660041 Krasnoyarsk, Russian Federation.*
[4]*Institute for Astronomy, University of Vienna, Türkenschanzstrasse 17, A-1180 Vienna, Austria*
[5]*IGAM/Institute of Physics, University of Graz, Universitätsplatz 5, A-8010 Graz, Austria*

Submitted to ApJ

Abstract

Planet atmospheric escape induced by high-energy stellar irradiation is a key **phenomenon** shaping the structure and evolution of planetary atmospheres. Therefore, the present-day properties of a planetary atmosphere are intimately connected with the amount of stellar flux received by a planet during its lifetime, thus with the evolutionary path of its host star. Using a recently developed analytic approximation based on hydrodynamic simulations for atmospheric escape rates, we track within a Bayesian framework the evolution of a planet as a function of stellar flux evolution history, constrained by the present-time mass and radius of its planets. We find that the ideal objects for this type of study are close-in sub-Neptune-like planets, as they are highly affected by atmospheric escape, and yet retain a significant fraction of their primordial hydrogen-dominated atmospheres. Furthermore, we apply this analysis to the HD3167 and K2-32 planetary systems. For HD3167, we find that the most probable irradiation level **at 150 Myr was between 40 and 130 times** solar, corresponding to a rotation period of $1.78^{+2.69}_{-1.23}$ days. For K2-32, we find a surprisingly low irradiation **level ranging between half and four times solar at 150 Myr.** Finally, we show that for multi-planet systems, our framework enables one to constrain poorly known properties of individual planets.

Key words: planets and satellites: atmospheres — planets and satellites: physical evolution — planets and satellites: gaseous planets — planets and satellites: individual (HD3167b, HD3167c, HD3167d, K2-32b, K2-32c, K2-32d)

1. Introduction

For late-type stars, rotation rate and high-energy radiation (X-ray and EUV below 912 Å; hereafter XUV) are intimately connected, with faster rotating stars being XUV brighter (e.g., Pallavicini et al. 1981; Pizzolato et al. 2003; Johnstone et al. 2015b). During their main-sequence lifetime, the rotation rate and XUV flux of late-type stars decrease with time. This evolution does not follow a unique path, as stars born with the same mass and metallicity can have widely different initial rotation rates, thus XUV fluxes (e.g., Mamajek & Hillenbrand 2008; Johnstone et al. 2015b). This non-uniqueness holds up to about 1 Gyr, at which point the evolutionary tracks of both rotation rate and XUV emission converge to one path (e.g., Tu et al. 2015). This implies that, for stars older than about 1 Gyr, it is not possible to infer their past XUV emission from their present stellar properties.

This problem becomes relevant when trying to understand the evolution of planetary atmospheres. The XUV stellar flux is absorbed in the upper atmosphere of planets leading to atmospheric expansion and eventually escape, which has been shown to occur efficiently on close-in Jupiter- and Neptune-mass planets (e.g., Vidal-Madjar et al. 2003; Fossati et al. 2010; Lecavelier des Etangs et al. 2012; Ehrenreich et al. 2015). Furthermore, atmospheric escape plays a significant role in shaping the observed exoplanet population and atmospheric properties (e.g., Lopez & Fortney 2013, 2014; Jin et al. 2014; Tian & Ida 2015; Owen & Wu 2017; Owen & Lai 2018; Jin & Mordasini 2018). Since in most cases atmospheric mass-loss rates are directly proportional to their XUV irradiation, escape is most effective when planets are young, thus the importance of knowing the past evolution of the stellar XUV radiation.

Corresponding author: Daria Kubyshkina
daria.kubyshkina@oeaw.ac.at

Luckily, for stars hosting close-in planets with hydrogen-dominated atmospheres, we can infer the stellar XUV irradiation tracks by modeling the planets' atmospheric evolution. The amount of XUV flux received by a planet during its lifetime determines the amount of hydrogen remaining in its envelope: since the radius of planets with masses below 0.35 Jupiter masses strongly correlates with its hydrogen envelope content (e.g., Lopez & Fortney 2014; Hatzes & Rauer 2015), the currently observed planetary radius constrains the past evolution of the stellar XUV emission.

Here, we present a framework, based on mass-loss rates extracted from hydrodynamic simulations (Kubyshkina et al. 2018b), **enabling the modeling of** the atmospheric evolution of super-Earths and sub-Neptunes that we apply to the HD3167 and K2-32 planetary systems. Section 2 summarises the algorithms and tools employed to compute the planetary atmospheric evolutionary tracks. Section 3 shows the results of tests conducted on mock systems. Section 4 presents the results **obtained for the HD3167 and K2-32 planetary systems**, while Section 5 gives our discussion and conclusions.

2. Atmospheric Evolution Model

To model the evolution of planetary atmospheres, we employ the scheme described by Kubyshkina et al. (2018b). Starting from a set of initial system parameters, as a planet loses mass from its hydrogen envelope, at each time-step the code extracts the atmospheric mass-loss rate from an analytical approximation based on a grid of hydrodynamic models, uses this value to update the atmospheric mass fractions, and estimates the planetary radius, which we then compare to the observed radius once the age of the system has been reached. Here, we summarise the key steps and describe the **applied improvements.**

There are three key ingredients: a model of the stellar flux evolutionary track, a model relating planetary parameters and atmospheric mass, and a model computing atmospheric escape rates.

For late-type stars, the stellar XUV flux out of the saturation regime depends on the stellar mass and rotation period, where the latter is time-dependent. Mamajek & Hillenbrand (2008) suggested the following analytical approximation for the evolution of the stellar rotation period (in days)

$$P_{\rm rot}(\tau) = 0.407\,[(B-V)_0 - 0.495]^{0.325}\,\tau^{0.566}, \qquad (1)$$

where τ is the stellar age (in Myr), and $(B-V)_0$ is the reddening-free stellar color. Equation (1) represents the average approximation based on a large set of late-type dwarfs. However, the evolutionary tracks for stellar rotation rates are non-unique (Johnstone et al. 2015b; Tu et al. 2015). To account for the different rotation-rate histories of different stars (i.e., from slow to fast rotator), we model the rotation period as a power law in τ, normalised such that the rotation period at the present age ($T_{\rm age}$) is consistent with the measured stellar rotation period ($P_{\rm rot}^{\rm now}$), obtaining

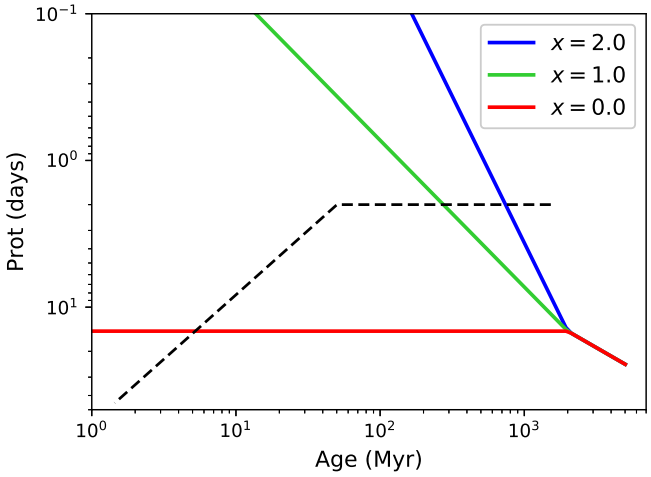

Figure 1. Model rotation-period curves as a function of age for a range of x values (colored solid curves). The black dashed curve denotes the time-dependent threshold when a star drops out of saturation, see Equation (2) and Figure 2 of Tu et al. (2015).

$$P_{\rm rot} = \begin{cases} P_{\rm rot}^{\rm now}\left(\frac{\tau}{T_{\rm age}}\right)^{0.566}, & \tau \geq 2\ {\rm Gyr} \\ P_{\rm rot}^{\rm now}\left(\frac{2{\rm Gyr}}{T_{\rm age}[{\rm Gyr}]}\right)^{0.566}\left(\frac{\tau[{\rm Gyr}]}{2{\rm Gyr}}\right)^{x}, & \tau < 2\ {\rm Gyr} \end{cases} \qquad (2)$$

where the exponent x is a positive value, typically ranging between 0 and ∼2, controlling the stellar rotation period at ages younger than 2 Gyr. Figure 1 shows examples of the parametric $P_{\rm rot}$ curves for a range of x values.

We then derive the stellar X-ray and EUV luminosity from the rotation period following Pizzolato et al. (2003) and Wright et al. (2011) that relate rotation rates and stellar masses to X-ray luminosity, including saturation effects for the fastest rotators, and Sanz-Forcada et al. (2011) relating X-ray and EUV fluxes. To account for variations of the stellar bolometric luminosity with time, we use the MESA Isochrones and Stellar Tracks (MIST, Paxton et al. 2018) model grid.

To estimate the planetary mass-loss rate at a given time, we use the analytic formulas provided by Kubyshkina et al. (2018c), which are based on a grid of one-dimensional hydrodynamic upper-atmosphere models (Kubyshkina et al. 2018b). The analytic approximation requires as input stellar XUV flux, planetary mass ($M_{\rm pl}$), radius ($R_{\rm pl}$), equilibrium temperature ($T_{\rm eq}$), and orbital separation (d_0).

To estimate the atmospheric mass of a planet $M_{\rm atm}$ as a function of planetary mass, radius, and $T_{\rm eq}$, we pre-compute $M_{\rm atm}$ following Johnstone et al. (2015) for the range of parameters used in Kubyshkina et al. (2018c), among which we further interpolate during an evolution run. For a given core mass, we determine the core radius $R_{\rm core}$ assuming an Earth-like density, as for planets with hydrogen-dominated envelopes the core composition has little influence on planetary size (e.g., Lopez & Fortney 2014; Petigura et al. 2016).

We combine these ingredients to compute the planetary atmospheric evolutionary tracks. For each run, we assume that the planetary orbital separation and stellar mass remain constant, and ignore the contribution of gravitational contraction and radioactive decay on the planetary $T_{\rm eq}$ during the first phases of evolution. We further assume that every planet accreted a hydrogen-dominated atmosphere from the proto-planetary nebula. We begin our simulations at 5 Myr, which is the typical lifetime of protoplanetary disks (Mamajek 2009). We also consider an initial planetary radius corresponding to a value of the restricted Jeans escape parameter Λ (computed for the planetary core mass and $T_{\rm eq}$ at the beginning of the simulation) of 5, where (Jeans 1925; Fossati et al. 2017)

$$\Lambda = \frac{G M_{\rm p} m_{\rm H}}{k_{\rm b} T_{\rm eq} R_{\rm p}}\,, \tag{3}$$

with G gravitational constant, $m_{\rm H}$ mass of an hydrogen atom, and $k_{\rm b}$ Boltzmann constant. **We come back to this point in Section 3.**

At each step of the evolution, first we compute the mass-loss rate based on the stellar flux and system parameters, which we use to update the atmospheric mass fraction, and the planetary radius. We adjust the time step, such that the change in atmospheric mass is less than 5% of $M_{\rm atm}$.

Finally, we use a Bayesian approach to constrain the evolutionary track of the stellar XUV luminosity fitting the currently observed planetary radius. To this end, we combine the planetary evolution model with the open-source Markov-chain Monte Carlo (MCMC) algorithm of Cubillos et al. (2017), **to compute** the posterior distribution for the stellar rotation rate **and the considered system parameters**.

For each MCMC run, we let the planetary mass, age of the system, present-time rotation period, orbital separation, and stellar mass as free parameters, with Gaussian-like priors according to the measured values and uncertainties. Within our scheme, we adopt a stellar radius from the MESA evolutionary tracks, which depends on the stellar mass. Similarly, we compute $T_{\rm eq}$ derived from the adopted stellar radius and d_0, assuming zero Bond albedo and full energy redistribution. The stellar radius may also be implicitly included in the computation in case only an upper limit for $P_{\rm rot}^{\rm now}$ has been given.

3. Validation

3.1. *Initial conditions*

Kubyshkina et al. (2018b) showed that for planets less massive than 6 $M_\oplus$ and orbital separations smaller than 0.1 AU, the initial radius has no impact on the final radius at the end of the evolution. This is because, for a given $M_{\rm pl}$ and d_0, **a larger (smaller) radius, hence larger (smaller) $M_{\rm atm}$, leads to a higher (lower) mass-loss rate.** Here, we look more thoroughly for the $M_{\rm pl}$ and d_0 values above which the atmospheric evolution drawn by our framework starts to become sensitive to the initial radius.

The main parameters controlling atmospheric escape at a given XUV irradiation and $R_{\rm pl}$ are $M_{\rm pl}$ and d_0. Therefore,

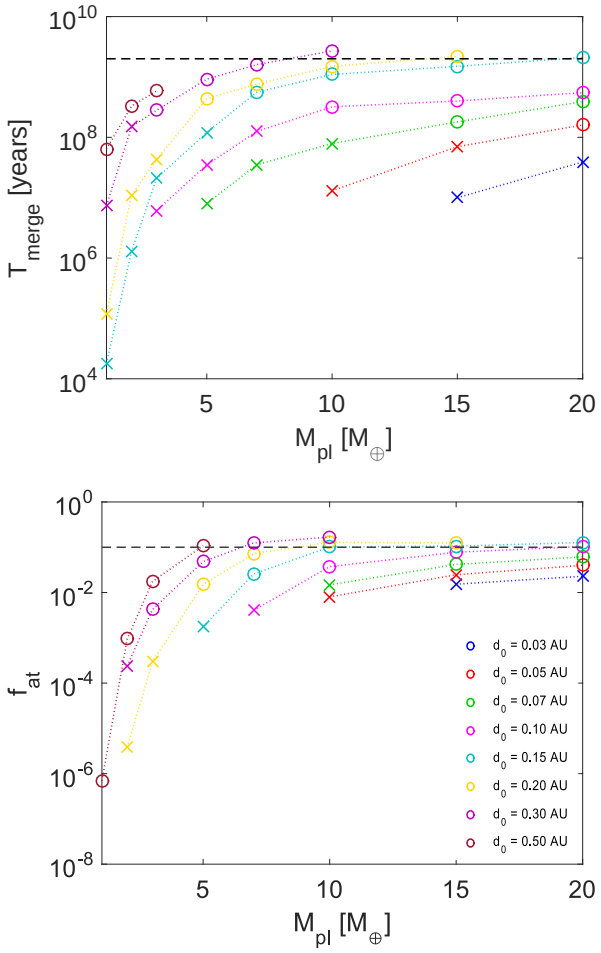

Figure 2. Top: time at which the planetary atmospheric evolutionary tracks merge as a function of $M_{\rm pl}$. Bottom: minimum initial atmospheric mass fraction for which the planetary atmospheric evolutionary tracks merge as a function of $M_{\rm pl}$. Colors indicate different orbital separations (see legend). Crosses and circles indicate whether the modelled planet loses or preserves a hydrogen-dominated atmosphere within 10 Gyr, respectively. For reference, the black dashed lines indicate in the top panel an age of 2 Gyr and in the bottom panel an atmospheric mass fraction of 10%.

we consider systems composed of a 0.8 $M_\odot$ medium rotator ($x = 1$) and planets with masses ranging between 1 and 20 $M_\oplus$ and orbital separations ranging between 0.02 and 0.50 AU. For each $M_{\rm pl}$–d_0 pair, we **computed** a series of evolutionary **tracks** over a range of initial planetary radii, looking for the time at which the evolutionary tracks merge ($T_{\rm merge}$), namely the atmospheric mass fractions become the same within 2%, and the minimum initial radius for which this happens.

We set the upper limit of the tested initial radii at 10 $R_\oplus$, the maximum $R_{\rm pl}$ available in the grid of upper atmosphere models (Kubyshkina et al. 2018b). We set the lower limit of the tested initial radii based on the minimum expected atmospheric mass fraction $f_{\rm at} = M_{\rm atm}/M_{\rm p}$. Since within the protoplanetary disc the mass of the initially accreted envelope grows with increasing planetary mass, we expect

Table 1. Radii and atmospheric mass fractions following a forward-model evolution for the test planets.

$R_{\rm pl}$ [$R_\oplus$] / $f_{\rm at}$ [%]	slow	medium	fast
b	3.44 ± 0.17 / 2.3 ± 0.8	2.80 ± 0.14 / $0.2^{+0.8}_{-0.2}$	2.71 ± 0.14 / $0.0^{+0.9}_{-0.0}$
c	5.26 ± 0.26 / $11.7^{+1.2}_{-1.0}$	4.12 ± 0.21 / $6.9^{+1.2}_{-1.3}$	3.22 ± 0.16 / $3.1^{+1.1}_{-1.3}$
d	6.53 ± 0.33 / $20.4^{+0.3}_{-1.0}$	4.53 ± 0.23 / $11.0^{+0.4}_{-0.8}$	3.40 ± 0.17 / $5.7^{+0.5}_{-0.7}$

$f_{\rm at} > 10^{-4}$ for $M_{\rm pl} \leq 5\,M_\oplus$ and $f_{\rm at} = 10^{-2}$ for higher masses (Stökl et al. 2015).

Figure 2 shows that $T_{\rm merge}$ increases with $M_{\rm pl}$ and d_0, and that it remains always below ∼2 Gyr. Figure 2 further shows the minimum atmospheric mass fraction $f_{\rm at,min}$ required for the evolutionary tracks to merge as a function of $M_{\rm pl}$ and d_0. Both $T_{\rm merge}$ and $f_{\rm at,min}$ increase with increasing $M_{\rm pl}$ and d_0. For systems with $M_{\rm pl}$ above $5\,M_\oplus$ and d_0 larger than 0.2 AU, $f_{\rm at,min}$ lies above the atmospheric mass fraction that can be expected to be originally accreted by each planet before the dispersal of the protoplanetary disc based on Stökl et al. (2015). Therefore, the results of the atmospheric evolution drawn by our framework start to become sensitive to the initial radius for planets more massive than $5\,M_\oplus$ and lying at orbital separations larger than 0.2 AU.

When applied to real cases, the results presented in Figure 2 should be considered as indicative. This is because the mass and rotation rate, thus XUV emission, of a given host star are possibly different from the values considered here. However, we can conclude that for sub-Neptune-like planets within 0.2 AU the initial conditions are in general not important, while for heavier and/or more distant planets this is not the case. We, however, evaluate in each case the impact of the choice of the initial conditions on the results.

3.2. *Reproducibility of mock systems*

To test whether and in which cases the retrieval approach can constrain the stellar XUV luminosity evolutionary tracks, we carry out an injection-retrieval test. To do so, we create a 5 Gyr old system, with a stellar mass (M_*) of $0.8\,M_\odot$ and $P_{\rm rot}^{\rm now} = 30$ days. We simulate three planets (labeled "b", "c", and "d") with masses of 20, 15, and $8\,M_\oplus$ at orbital separations of 0.05, 0.1, and 0.2 AU, respectively. These parameters make sure that the initial planetary radius, set as the value for which $\Lambda = 5$, has no influence on the results. The core radii of the three planets are 2.71, 2.47, and $2.00\,R_\oplus$, respectively.

3.2.1. *Typical uncertainties*

To estimate the system-parameter uncertainties, we look at the typical measured uncertainties listed in the NASA Exoplanet Archive[1]. For planets similar to those considered in this test (i.e., $M_{\rm pl}$ below $25\,M_\oplus$, $T_{\rm eq}$ between 300 and 2000 K, stellar mass between 0.4 and $1.3\,M_\odot$, and constrained planetary masses), we adopt stellar-mass uncertainties of 4% (signal-to-noise ratio, S/N, of 25), orbital-separation uncertainties of 1.5% (S/N = 66.7), planetary-mass uncertainties of 20% (S/N = 5), and stellar-age uncertainties of 30% (S/N = 3.3). Note that the estimated age uncertainties vary significantly; however, this uncertainty has the largest influence only for systems much younger than the focus of this work (see below).

Finally, for the measured rotation period it is not possible to reliably associate a typical uncertainty because the number of stars for which $P_{\rm rot}^{\rm now}$ has been measured is small, and in most cases $P_{\rm rot}^{\rm now}$ either corresponds just to an upper limit or has been estimated from approximations, such as that of Mamajek & Hillenbrand (2008). On the basis of the few stars for which $P_{\rm rot}^{\rm now}$ has been measured, we adopt an uncertainty of 15% (S/N ≈ 6.7).

3.2.2. *Results*

We simulate three evolution scenarios with $x = 0.1$, 0.566, and 1.5, corresponding to an initially "slow", "medium", and "fast" rotator or alternatively rotational periods at 150 Myr ($P_{\rm rot}^{150}$) of 13.8, 4.1, and 0.4 days, respectively. The planetary radii and atmospheric mass fractions (accounting for the uncertainties on the parameters) obtained for these scenarios and for planets "b", "c", and "d" following a forward model are listed in Table 1. When orbiting a medium or a fast rotator, planet "b" loses (almost) completely its atmosphere as, within the uncertainties, its atmospheric mass fraction remains below 1.0%.

As a typical example of the results obtained for the test systems, Figure 3 shows the MCMC posterior distributions for the case of the "c" planet orbiting the medium rotator. The results obtained for the other tests are shown in the Appendix (Figures 9–16).

In Figure 3, the top row shows the posterior distribution obtained when all system parameter were set free. To identify whether there are dominant parameters driving the results and which ones they are, we repeated the analysis fixing one parameter at a time. For completeness, we run a test fixing all parameters except for the planetary radius, recovering the injected $P_{\rm rot}$ distribution.

For each modelled case, the posterior distribution for the stellar rotation period matches the injected value within the 68% highest posterior density (HPD) credible interval. Our tests indicate that planetary mass is the main parameter influencing the posterior distribution of the rotation period, with the other parameters playing a minor role.

Our tests also show that the posterior distribution of all parameters, except for the planetary mass, are consistent

[1] http://exoplanetarchive.ipac.caltech.edu

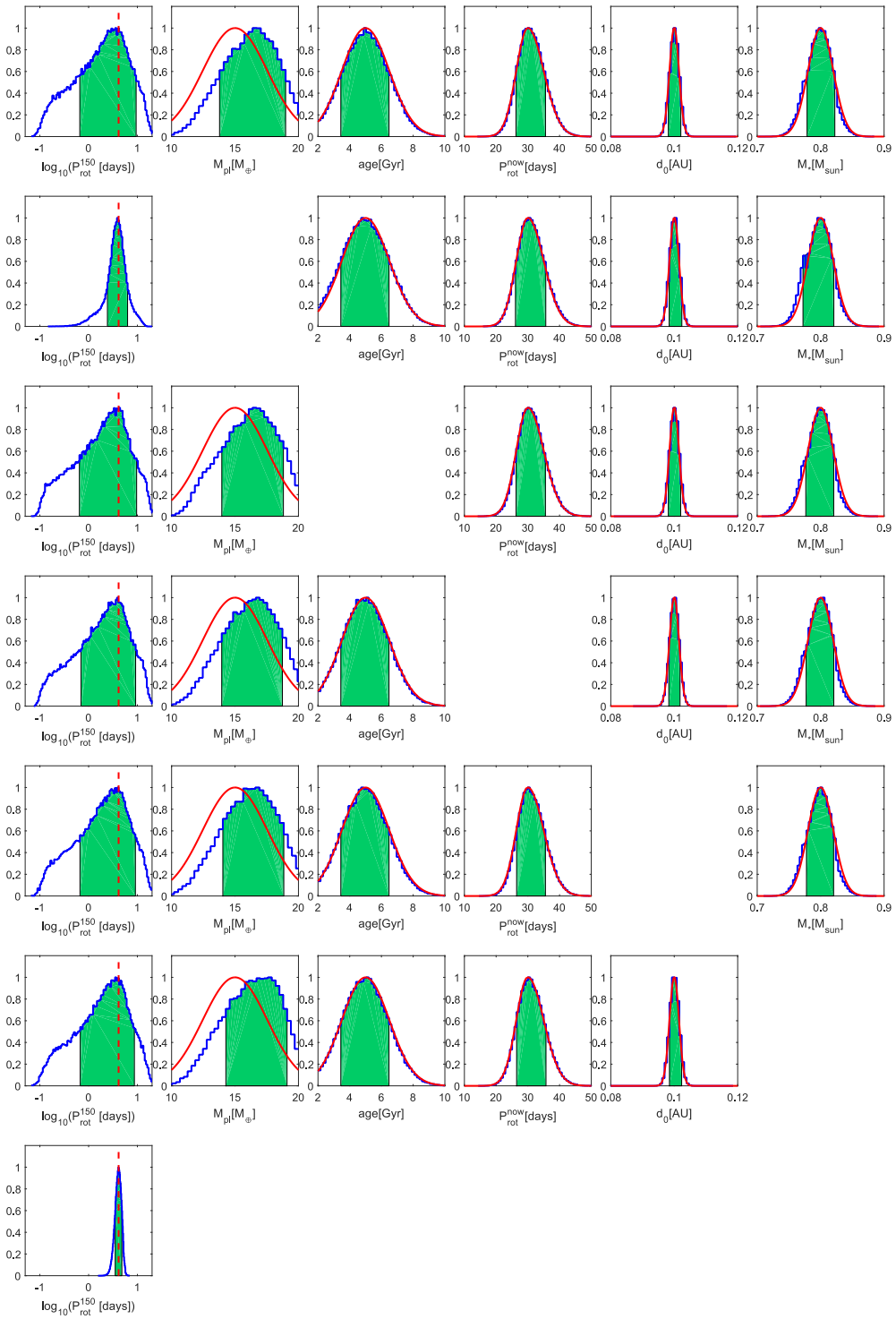

Figure 3. Posterior distributions for the injection-retrieval runs described in Section 3.2 for the test planet "c" orbiting a medium rotator. From left to right, each column shows the posterior distribution for the stellar rotation period at 150 Myr ($P_{\rm rot}^{150}$), planetary mass, age of the system, present-time rotation period, orbital separation, and stellar mass, respectively. From top to bottom, each row shows the results assuming all system parameters free, and then fixing one of these parameters at a time, respectively. The missing panels indicate the parameter that has been fixed in each run. The bottom row, composed by a sole panel, shows the posterior stellar rotation period at 150 Myr while fixing all input parameters, except for the planetary radius. The green shading denotes the 68% highest posterior density (HPD) credible intervals. The red dashed vertical lines in the left column show the injected $P_{\rm rot}^{150}$ value, whereas the red solid lines show the prior distributions of the input parameters.

with the input distribution. For the planetary mass, but we find that the posterior distributions are consistently shifted towards higher values than their prior distributions; however, the results are consistent within 1σ with the prior. The pair-wise posterior distributions (Figure 4) reveal a well-defined degeneracy between $P_{\rm rot}^{150}(M_{\rm pl})$ and $M_{\rm pl}$, which occurs because one can arrive at the same planetary radius through a lower (higher) planetary mass and a slower (faster) rotator, thus lower (higher) past XUV irradiation. This explains the shift between prior and posterior distributions. This effect is more evident for closer-in planets and for slower rotators. In the case of the slow-rotator simulation, we also find a slight shift of the posterior of the stellar rotation period compared to the injected value, but still lying well within 1σ. This indicates that the algorithm prefers to reach the final planetary radius with a slightly heavier planet and a slightly faster rotator.

For the planets orbiting the fast rotator, the posteriors for planetary mass are narrower than the prior. This happens also for the test planet "b", which is the closer-in of the three, orbiting the medium rotator (Figure 12), for which the final atmospheric mass fraction is below 1%. This happens because the thin atmosphere remaining at the end of the simulation can be obtained only through a narrow range of planetary masses. This indicates that our model imposes constraints on the plausible physical parameters of the system, leading to constraints on the planetary masses.

The left and middle panels of Figure 4 show the pair-wise posterior distributions of $P_{\rm rot}^{150}$ vs. $M_{\rm pl}$ and $T_{\rm age}$ vs. $M_{\rm pl}$, for the [medium-rotator] case when all parameters are free. The correlation is rather narrow, meaning that, despite the whole range of possible stellar rotation rates is wide, at each given planetary mass the range of possible stellar rotation rates is narrow. For the case of the slow rotator, we also find a correlation between $M_{\rm pl}$ and $T_{\rm age}$. This occurs because the atmospheric mass fraction changes more slowly over time for the slow rotator. A correlation between $P_{\rm rot}^{150}$ and $T_{\rm age}$ is the direct consequence of the other two correlations (right panel of Figure 4). The other system parameters do not show significant correlations.

For some of the test planets, such as planets "b" and "c" orbiting the fast rotator, we obtained broad posterior distributions, thus weak constraints on the stellar rotation rate history. The case of planet "b", the closer-in and most massive planet, orbiting the fast or medium rotator lead to the (almost) complete escape of the atmosphere. Therefore, even though formally the injected value of the rotation period lays within the 68% HPD credible interval, we can just obtain an upper limit for the stellar rotation period. Our tests indicate that for planets with a thin hydrogen envelope, a meaningful use of our scheme requires a high accuracy of the system parameters: the thinner the hydrogen atmosphere, the higher the required accuracy on the system parameters.

To make sure that our results do not depend on the adopted masses and positions of the test planets, we carry out additional runs considering test planets orbiting at distances from the host star ranging between 0.1 and 0.25 AU and having masses ranging between 5 and 20 $M_\oplus$. The results of these tests, not shown here, are consistent with those presented above, confirming that the accuracy with which we are able to constrain the stellar rotation period depends mainly on the accuracy with which the system parameters have been measured.

3.2.3. *Influence of the uncertainties*

From the test runs, illustrated in Figures 3 and 9–16, we expect that the main uncertainties affecting our ability to constrain the stellar rotation history are those on $M_{\rm pl}$ and $R_{\rm pl}$. Therefore, we performed additional tests to examine how the results change by changing the uncertainties on these parameters. For the planetary radius, we varied the uncertainty between 2 and 50%, while for the planetary mass, we varied the uncertainty between 5 and 50%. In addition, because of the large spread with which ages of planetary systems are derived, we present the results of additional runs made considering age uncertainties of 50 and 100%.

Figure 5 shows the results of these tests. The top-left panel is the reference distribution, which coincides with the top-left panel of Figure 3. The first, second, and third columns present the results obtained varying the uncertainties on the system's age, planetary radius, and planetary mass, respectively. There is little variation in the resulting posterior distributions for $P_{\rm rot}^{150}$ when varying the system's age uncertainty, because the main changes in atmospheric mass fraction occur during the early stages of evolution—before 2 Gyr. Therefore, the uncertainty on the system's age plays a role only for very young systems. As expected, increasing the uncertainty on the planetary radius and mass broadens the posterior distribution of $P_{\rm rot}^{150}$, becoming nearly flat for a radius and/or mass uncertainties of 50% (not shown). Improving the planetary-mass uncertainty has the largest impact on the expected $P_{\rm rot}^{150}$ posterior distribution. For the real planets examined in this study, the uncertainties on planetary masses are 13–16%.

3.2.4. *Simultaneous modelling of multiple planets in the same system*

Here we explore what can be obtained by analysing simultaneously two or more planets orbiting the same star. Figure 6 shows the posterior distributions for $P_{\rm rot}^{150}$ obtained by simultaneously modelling the "b", "c", and "d" test planets orbiting a slow, medium, and fast rotator. For comparison, Figure 6 further shows the distributions obtained analysing the planets separately. As one can expect, considering simultaneously multiple planets narrows, and thus improves, the results. This can be best seen in the middle panel (i.e., medium rotator), where the innermost planet constrains the upper boundary of $P_{\rm rot}^{150}$,

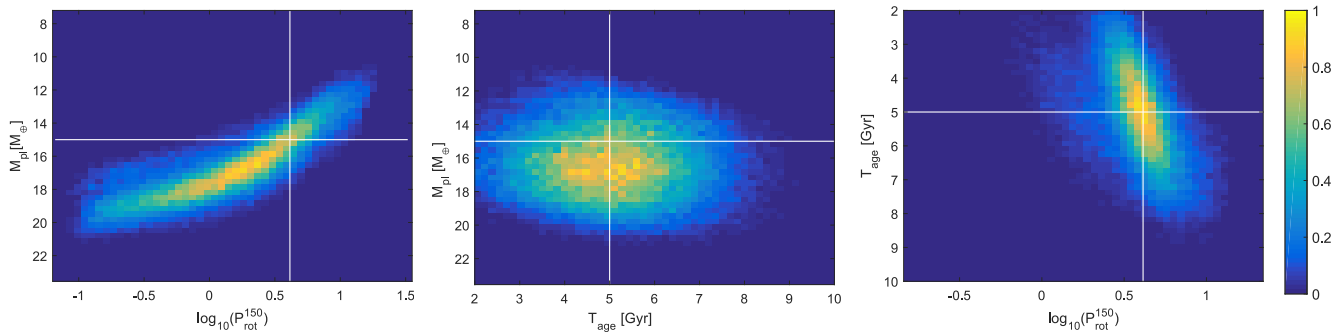

Figure 4. Pair-wise posterior distributions of $P_{\rm rot}^{150}$ vs $M_{\rm pl}$ (left), system's age vs $M_{\rm pl}$ (middle), and $P_{\rm rot}^{150}$ vs system's age, the latter with $M_{\rm pl}$ fixed (right), for the test planet "c" orbiting the medium rotator. The white solid lines indicate the injected values.

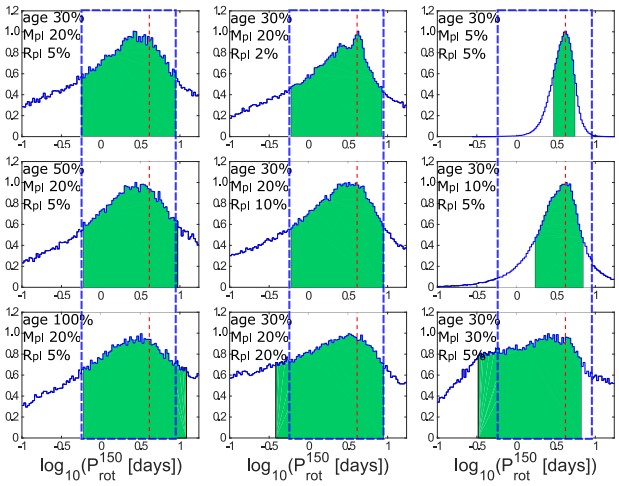

Figure 5. Posterior distribution of the rotation period at an age of 150 Myr for the test planet "c" orbiting the medium rotator. The different panels present the results obtained following different assumptions on the uncertainties of the parameters, as labelled on the top-left corner of each panel. The blue dashed rectangles show for reference the width of the 68% HPD credible interval for the test reference uncertainties (top-left panel).

while the outer planets constrains the lower boundary of $P_{\rm rot}^{150}$, and in the right panel, for which the final distribution is significantly narrower.

The mock system we used here has been constructed in such a way that the uncertainties on the planetary parameters are homogeneous among the three planets. However, this is unlikely to be the case for real systems. Therefore, we expect that a meaningful simultaneous analysis of multi-planet systems requires that the masses and radii of the planets considered in the analysis have sufficiently low uncertainties.

4. Application to Observed Planetary Systems

We now apply our atmospheric evolution framework to the HD3167 and K2-32 planetary systems aiming at estimating the rotation rate evolution of their host stars. Table 2 lists the adopted system parameters and results.

4.1. *HD 3167*

The HD3167 planetary system is composed of three sub-Neptune-mass planets, where the innermost (HD3167b) and outermost (HD3167c) planets transit their host star (Vanderburg et al. 2016; Gandolfi et al. 2017; Christiansen et al. 2017). All planets in the system **have masses derived from radial-velocity measurements.**

HD3167b has a measured average density consistent with a rocky composition, suggesting that the planet has lost its primordial hydrogen-dominated atmosphere (Gandolfi et al. 2017). We indeed find that the hydrogen envelope of HD3167b escapes completely within the first 0.01 Myr for **any reasonable x value (i.e., $0 < x < 2$).**

HD3167c has an average density of $\sim$2 g cm^{-3}, suggesting that the planet still retains part of its primary hydrogen-dominated atmosphere. The evolutionary tracks do not depend on the initial conditions, except for a slow rotator and a planetary mass above 10.9 $M_\oplus$, for which the atmospheric evolutionary tracks merge at $f_{\rm at} \approx 7\times10^{-2}$ and at an age of $\approx$1 Gyr. **Figure 7 shows the posterior distributions obtained adopting the system parameters given by Christiansen et al. (2017), indicating that the host star was likely to be a fast to moderate rotator. In particular, we obtain that at 150 Myr the star emitted 38–128 times the XUV flux of the current Sun, with an upper limit being more likely, since it is a saturation value corresponding to all periods below 2 days. The pair-wise posterior distributions of the parameters involved in the modeling are shown in Appendix (Figure 17). We run the simulations again adopting the system parameters of Gandolfi et al. (2017) obtaining consistent results, except for a slightly broader $P_{\rm rot}^{150}$ posterior distribution towards larger values (i.e., slower rotator) due to the lower planetary mass.**

HD3167d is not transiting and therefore does not have a measured radius. Nevertheless, the stellar rotation rate evolutionary tracks based on the results obtained from HD3167c lead us to constrain the possible atmospheric evolution of HD3167d suggesting that the planet should have completely lost its primary, hydrogen-dominated atmosphere within 0.02–1.48 Gyr.

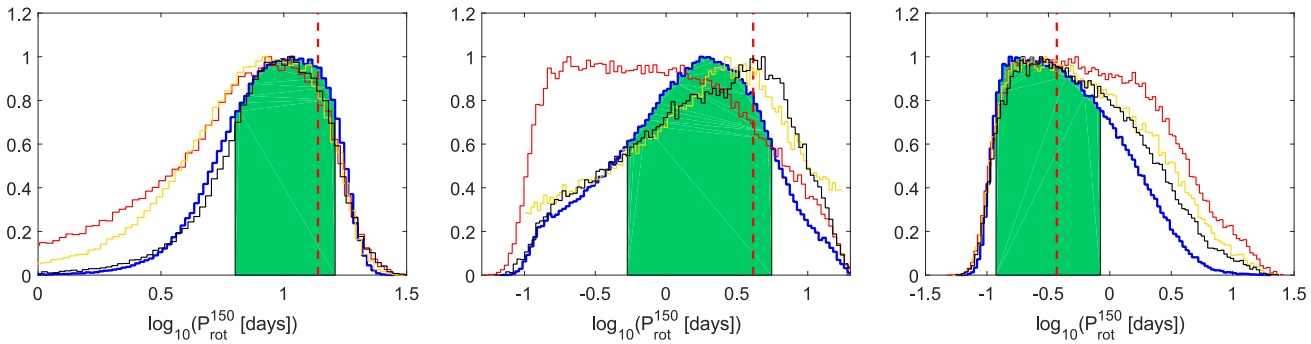

Figure 6. Results of the simultaneous modelling of the three test planets orbiting a slow (left), medium (middle), and fast (right) rotator. The red, yellow, and black thin lines show the posterior distributions obtained by modelling separately the "b", "c", and "d" planets, respectively.

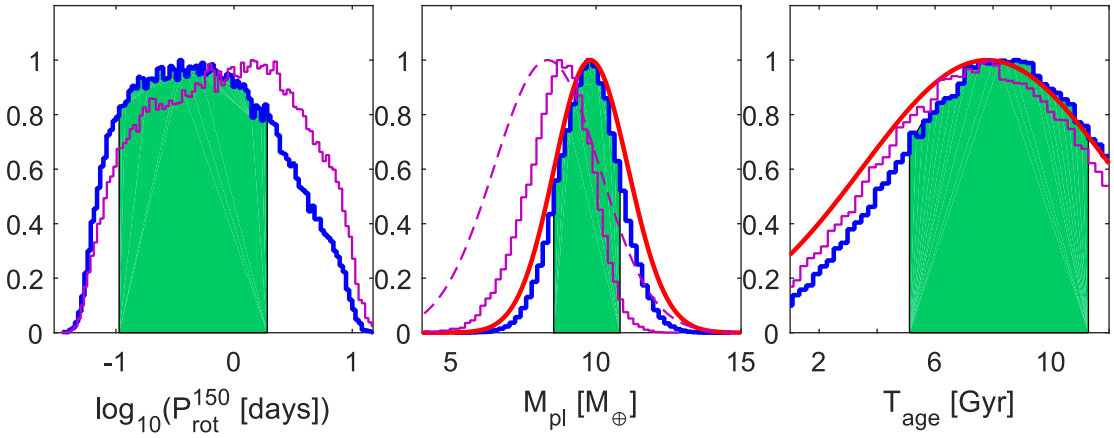

Figure 7. MCMC posterior distributions **for** $P_{\rm rot}^{150}$, $M_{\rm pl}$**, and system's age obtained from the modeling of HD3167c based on the data from Christiansen et al. (2017).** The shaded areas correspond to the 68% HPD credible interval. **The violet solid lines show the same distributions obtained considering the system parameters given by Gandolfi et al. (2017), while the violet dashed line shows the assumed** $M_{\rm pl}$ **prior.**

4.2. *K2-32*

The K2-32 planetary system is composed of three transiting sub-Neptune-mass planets. Radial-velocity measurements placed loose constraints on the planetary masses (Dai et al. 2016; Petigura et al. 2017): K2-32c has an upper-mass limit, whereas for K2-32d the mass is measured with a 50% uncertainty. Therefore, we focused our analysis on K2-32b, which has a low average density of $0.67\pm0.16\,{\rm g\,cm^{-3}}$, strongly indicative of the presence of an extended hydrogen envelope. For the analysis, we consider the system parameters given by Petigura et al. (2017).

Our results (Figure 8) strongly favor the slow rotator scenario with the posterior distribution indicating $P_{\rm rot}^{150}$ **values lying between 10 and 26 days, which coincides with the slow rotation edge of the distribution given by Johnstone et al. (2015b), and corresponds to XUV fluxes at 150 Myr between 0.5 and 4.0 times those of the present Sun. This means that, within our framework, the existence of such a close-in, low-density planet is possible only if the star has always been a very slow rotator. The pairwise posterior distributions of the parameters involved in the modeling are shown in Appendix (Figure 18).**

Given the weak mass constraints for K2-32c and K2-32d, we used the results on the stellar rotation rate history obtained from the analysis of K2-32b to place further constraints on the **estimated planetary masses.** The low measured average density of K2-32d ($1.38^{+0.92}_{-0.67}\,{\rm g\,cm^{-3}}$) suggests that the planet has a significant hydrogen-dominated envelope. Assuming the range of possible stellar rotation rates found from the analysis of K2-32b, we expect the mass of K2-32d to range **between 5.60 and 6.87** $M_\oplus$.

For K2-32c, by adopting a mass equal to the upper mass limit and the results on the stellar rotation rate derived from K2-32b, we obtain a planetary radius significantly larger than the measured one, with the planet retaining nearly 50% of its initial envelope. **To fit the observed** $R_{\rm pl}$**, we require planetary masses ranging between 4.55 and 7.29** $M_\oplus$**. By adopting instead the planetary radius given**

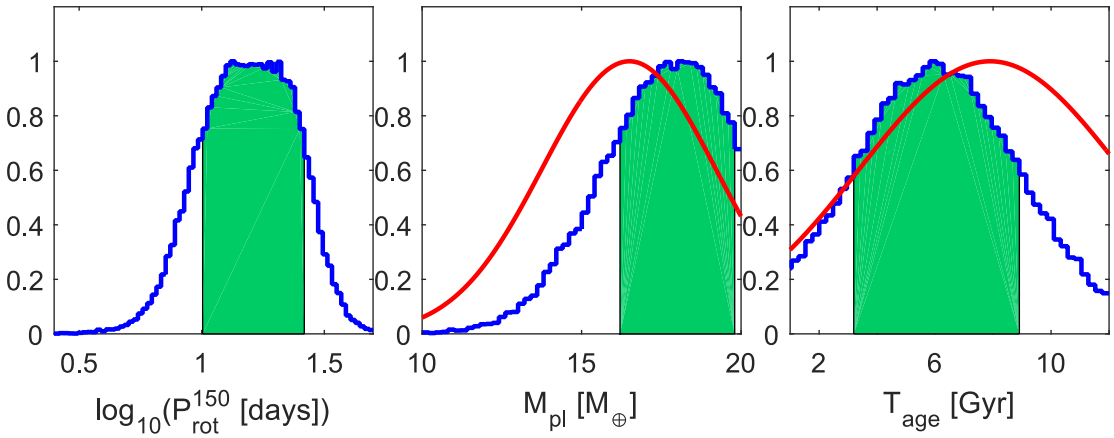

Figure 8. Same as Figure 7, but for K2-32b.

by Mayo et al. (2018), the range of possible planetary masses shifts slightly towards larger values, namely 4.76–7.52 $M_\oplus$.

5. Discussions and conclusions

The currently observed atmospheric properties of exoplanets strongly depend on their mass-loss history, which can reveal the otherwise unknown evolution history of the stellar high-energy radiation. We developed a framework to compute planetary radii as a function of time and coupled it to a Bayesian sampler to infer the rotation rate history of the host star, which is constrained by the measured basic system parameters. We applied this framework to the HD3167 and K2-32 systems.

Despite having very similar masses, we find that the K-type stars HD3167 and K2-32 had a widely different initial rotation-rate, thus high-energy emission. Most likely, HD3167 evolved as a medium (or fast) rotator, while K2-32 evolved as an extremely slow rotator. We further showed that our evolution model can lay further constraints for planetary systems in which some of **the planetary parameters are** poorly measured. For the K2-32 system, the stellar rotation rate constrained by K2-32b, leads to masses of K2-32c ranging between 4.55 and 7.52 $M_\oplus$, while for K2-32d we derive masses ranging between 5.60 and 6.87 $M_\oplus$.

We have shown that atmospheric evolution modeling of close-in planets has the power to uncover the past rotation history of late-type stars. **It enables one also to constrain poorly known parameters (i.e., mass and/or radius) of some of the planets in a system.** These results can be extended to other systems provided that they host a close-in planet with a mass close to that of Neptune or smaller and with a hydrogen-dominated envelope. **A systematic analysis of a large sample of systems will also help to set constraints on the different model assumptions adopted by this framework. Furthermore, by comparing the output stellar rotation period distribution at a given age with what measured in clusters, or by comparing the results obtained from two planets in a system, it would be possible to identify planets that evolved differently from what expected. These planets might have been affected, for example, by strong impacts, or experienced an early dispersal of the protoplanetary nebula, or underwent strong hydrogen release from the solidifying rocky core (e.g., Chachan & Stevenson 2018; Bonomo et al. 2019). Firmly identifying these "odd" systems would be the first step towards studying them to better understand the evolution of planetary systems.**

Our results show also the importance of precisely constraining system parameters, particularly **the system's age and planetary mass and radius**. The ESA *PLATO* mission (Rauer et al. 2014) will be in the best position to simultaneously discover transiting planetary systems and provide system parameters with the necessary accuracy to pin down the evolutionary track of the planetary atmosphere and stellar rotation rate.

We acknowledge the FFG project P853993, the FWF/NFN projects S11607-N16 and S11604-N16, and the FWF projects P27256-N27 and P30949-N36. NVE acknowledges support by the Russian Science Foundation grant No 18-12-00080. **We thank the anonymous referee for insightful comments.**

References

Berger, T. A., Huber, D., Gaidos, E., & van Saders, J. L. 2018, ApJ, 866, 99
Bonomo, A. S., Zeng, L., Damasso, M., et al. 2019, Nature Astronomy,
Chachan, Y., & Stevenson, D. J. 2018, ApJ, 854, 21
Christiansen, J. L., Vanderburg, A., Burt, J., et al. 2017, AJ, 154, 122
Crossfield, I. J. M., Ciardi, D. R., Petigura, E. A., et al. 2016, ApJS, 226, 7
Cubillos, P., Harrington, J., Loredo, T. J., et al. 2017, AJ, 153, 3
Dai, F., Winn, J. N., Albrecht, S., et al. 2016, ApJ, 823, 115
Ehrenreich, D., Bourrier, V., Wheatley, P. J., et al. 2015, Nature, 522, 459

Fossati, L., Erkaev, N. V., Lammer, H., et al. 2017, A&A, 598, A90
Fossati, L., Haswell, C. A., Froning, C. S., et al. 2010, ApJL, 714, L222
Gandolfi, D., Barragán, O., Hatzes, A. P., et al. 2017, AJ, 154, 123
Hadden, S., & Lithwick, Y. 2017, AJ, 154, 5
Hatzes, A. P., & Rauer, H. 2015, ApJL, 810, L25
Jeans, J. 1925, The Dynamical Theory of Gases. By Sir James Jeans. Cambridge University Press, 1925. ISBN: 978-1-1080-0564-7
Jin, S., Mordasini, C., Parmentier, V., et al. 2014, ApJ, 795, 65
Jin, S., & Mordasini, C. 2018, ApJ, 853, 163
Johnstone, C. P., Güdel, M., Stökl, A., et al. 2015, ApJL, 815, L12
Johnstone, C. P., Güdel, M., Brott, I., & Lüftinger, T. 2015, A&A, 577, A28
Kubyshkina, D., Fossati, L., Erkaev, N. V., et al. 2018b, A&A, 619, A151
Kubyshkina, D., Fossati, L., Erkaev, N. V., et al. 2018c, ApJL, 866, L18
Lecavelier des Etangs, A., Bourrier, V., Wheatley, P. J., et al. 2012, A&A, 543, L4
Lopez, E. D., & Fortney, J. J. 2013, ApJ, 776, 2
Lopez, E. D., & Fortney, J. J. 2014, ApJ, 792, 1
Mamajek, E. E., & Hillenbrand, L. A. 2008, ApJ, 687, 1264-1293
Mamajek, E. E. 2009, American Institute of Physics Conference Series, 1158, 3
Masuda, K., Hirano, T., Taruya, A., Nagasawa, M., & Suto, Y. 2013, ApJ, 778, 185
Mayo, A. W., Vanderburg, A., Latham, D. W., et al. 2018, AJ, 155, 136
Morton, T. D., Bryson, S. T., Coughlin, J. L., et al. 2016, ApJ, 822, 86
Owen, J. E., & Wu, Y. 2017, ApJ, 847, 29
Owen, J. E., & Lai, D. 2018, MNRAS, 479, 5012
Pallavicini, R., Golub, L., Rosner, R., et al. 1981, ApJ, 248, 279
Paxton, B., Schwab, J., Bauer, E. B., et al. 2018, ApJS, 234, 34
Petigura, E. A., Howard, A. W., Lopez, E. D., et al. 2016, ApJ, 818, 36
Petigura, E. A., Sinukoff, E., Lopez, E. D., et al. 2017, AJ, 153, 142
Pizzolato, N., Maggio, A., Micela, G., Sciortino, S., & Ventura, P. 2003, A&A, 397, 147
Rauer, H., Catala, C., Aerts, C., et al. 2014, Experimental Astronomy, 38, 249
Sanz-Forcada, J., Micela, G., Ribas, I., et al. 2011, A&A, 532, A6
Stökl, A., Dorfi, E., & Lammer, H. 2015, A&A, 576, A87
Tian, F., & Ida, S. 2015, Nature Geoscience, 8, 177
Tu, L., Johnstone, C. P., Güdel, M., & Lammer, H. 2015, A&A, 577, L3
Vanderburg, A., Bieryla, A., Duev, D. A., et al. 2016, ApJL, 829, L9
Vidal-Madjar, A., Lecavelier des Etangs, A., Désert, J.-M., et al. 2003, Nature, 422, 143
Weiss, L. M., Marcy, G. W., Rowe, J. F., et al. 2013, ApJ, 768, 14
Wright, N. J., Drake, J. J., Mamajek, E. E., & Henry, G. W. 2011, ApJ, 743, 48

Table 2. Adopted system parameters and obtained results (x) for HD3167 and K2-32. The cases for which $R_{\rm pl}$ reaches the core radius are given in parenthesis.

planet	M_*	age	$P_{\rm rot}$	$M_{\rm pl}$	$R_{\rm pl}$	ρ	d_0	Λ	x
	$[M_\odot]$	[Gyr]	[days]	$[M_\oplus]$	$[R_\oplus]$	[g/cm^3]	[AU]		
HD3167b	0.88 ± 0.02	7.8 ± 4.3	23.52 ± 2.87	5.69 ± 0.44 (a)	1.57 ± 0.05 (a)	$8.00^{+1.10}_{-0.98}$	0.01752 ± 0.00063	15.1	–
				5.02 ± 0.38 (b)	$1.70^{+0.18}_{-0.15}$ (b)	$5.60^{+2.15}_{-1.43}$		12.3	
					1.56 ± 0.06 (c)				
					$1.62^{+0.17}_{-0.08}$ (d)				
HD3167c	0.88 ± 0.02	7.8 ± 4.3	23.52 ± 2.87	$8.33^{+1.79}_{-1.85}$ (a)	$2.74^{+0.11}_{-10}$ (a)	$2.21^{+0.56}_{-0.53}$	0.1806 ± 0.0080	39.7	$1.32^{+1.72}_{-0.89}$
				$9.80^{+1.30}_{-1.24}$ (b)	$3.01^{+0.42}_{-0.28}$ (b)	$1.97^{+0.94}_{-0.59}$		42.6	$1.08^{+0.98}_{-0.65}$
					$2.85^{+0.24}_{-0.15}$ (c)				
					$2.83^{+0.31}_{-0.14}$ (d)				
HD3167d	0.88 ± 0.02	7.8 ± 4.3	23.52 ± 2.87	6.90 ± 0.71 (b)	$(1.90 \pm 0.07)^*$	–	0.07757 ± 0.00027	–	–
K2-32b	0.86 ± 0.03	7.90 ± 4.50	$61.10^{+3.18}_{-2.53}$	16.50 ± 2.70 (e)	5.13 ± 0.28 (e)	0.67 ± 0.16	0.08036 ± 0.00088	29.1	≥ 3.82
				21.10 ± 5.90 (f)	5.13 ± 0.28 (f)	0.67 ± 0.16		37.2	
					5.62 ± 0.45 (g)				
					$5.17^{+0.20}_{-0.16}$ (d)				
K2-32c	0.86 ± 0.03	7.90 ± 4.50	$61.10^{+3.18}_{-2.53}$	< 12.10 (e)	3.01 ± 0.25 (e)	< 2.70	0.1399 ± 0.0015	< 48.0	–
				< 8.1 (f)	$3.48^{+0.97}_{-0.42}$ (f)	< 1.10		< 27.8	
					3.32 ± 0.33 (g)				
					$3.12^{+0.18}_{-0.12}$ (d)				
K2-32d	0.86 ± 0.03	7.90 ± 4.50	$61.10^{+3.18}_{-2.53}$	10.30 ± 4.70 (e)	3.43 ± 0.35 (e)	$1.38^{+0.92}_{-0.67}$	0.1862 ± 0.0020	41.6	–
				< 35.00 (f)	3.75 ± 0.40 (f)	< 3.60		< 129	
					3.77 ± 0.41 (g)				
					$3.41^{+0.26}_{-0.14}$ (d)				

a – Gandolfi et al. (2017), b – Christiansen et al. (2017), c – Vanderburg et al. (2016), d – Mayo et al. (2018), e – Petigura et al. (2017), f – Dai et al. (2016), g – Crossfield et al. (2016), h – Weiss et al. (2013), i – Morton et al. (2016), j – Berger et al. (2018), k – Masuda et al. (2013), l – Hadden & Lithwick (2017).

* – the **radius derived in** this paper assuming the rotation rate obtained for HD 3167 c.

APPENDIX

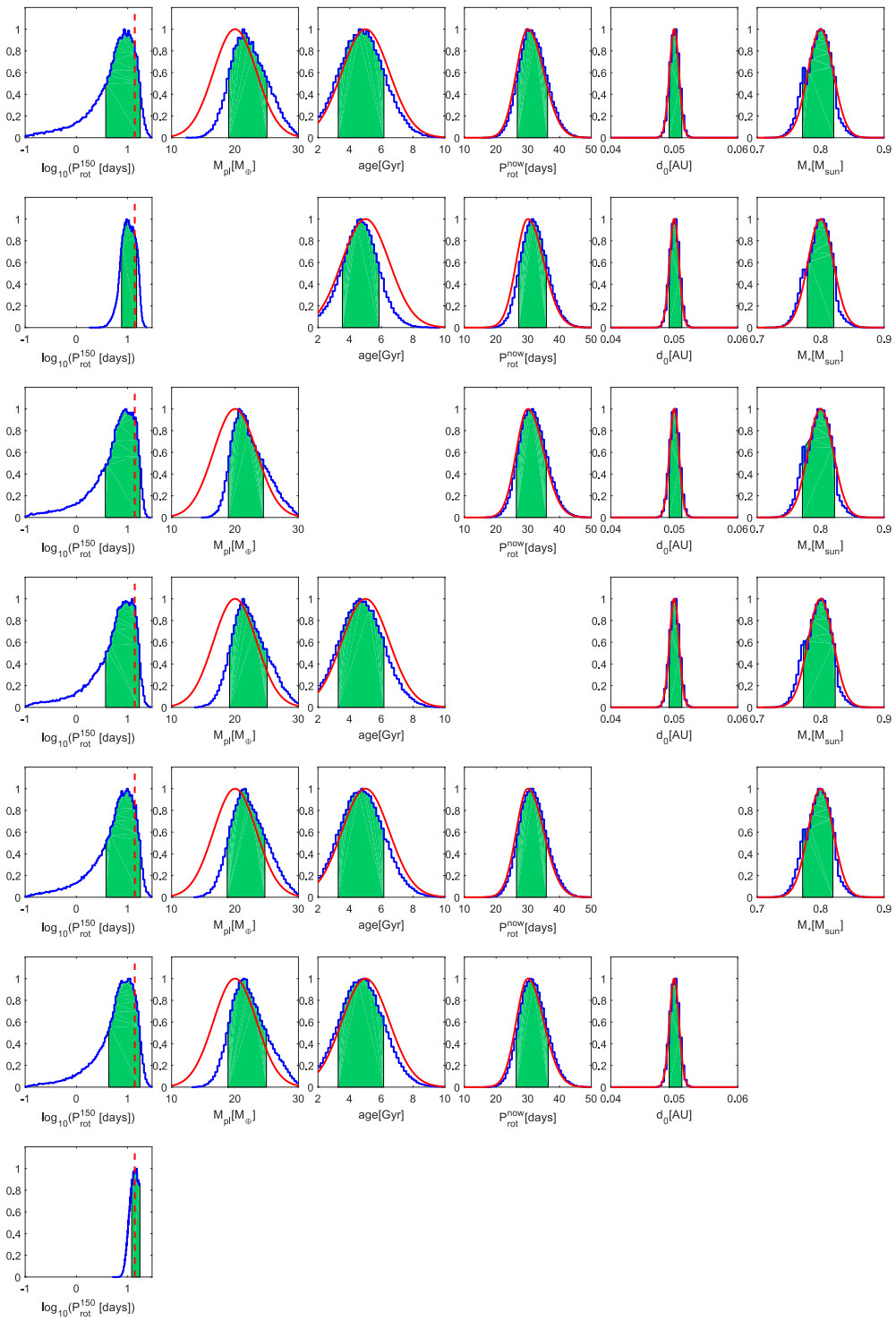

Figure 9. Same as Figure 3, but for the test planet "b" orbiting a slow rotator.

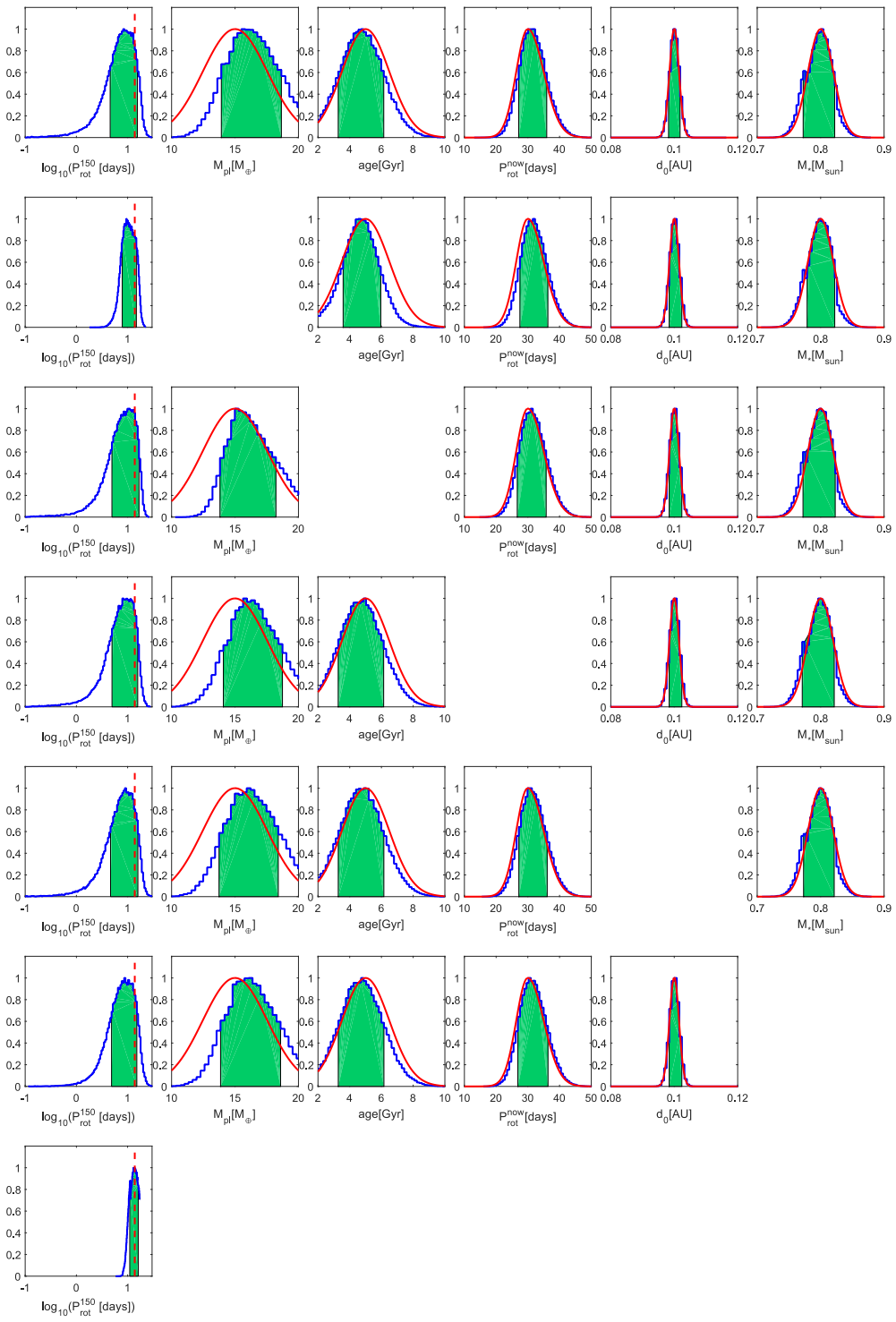

Figure 10. Same as Figure 3, but for the test planet "c" orbiting a slow rotator.

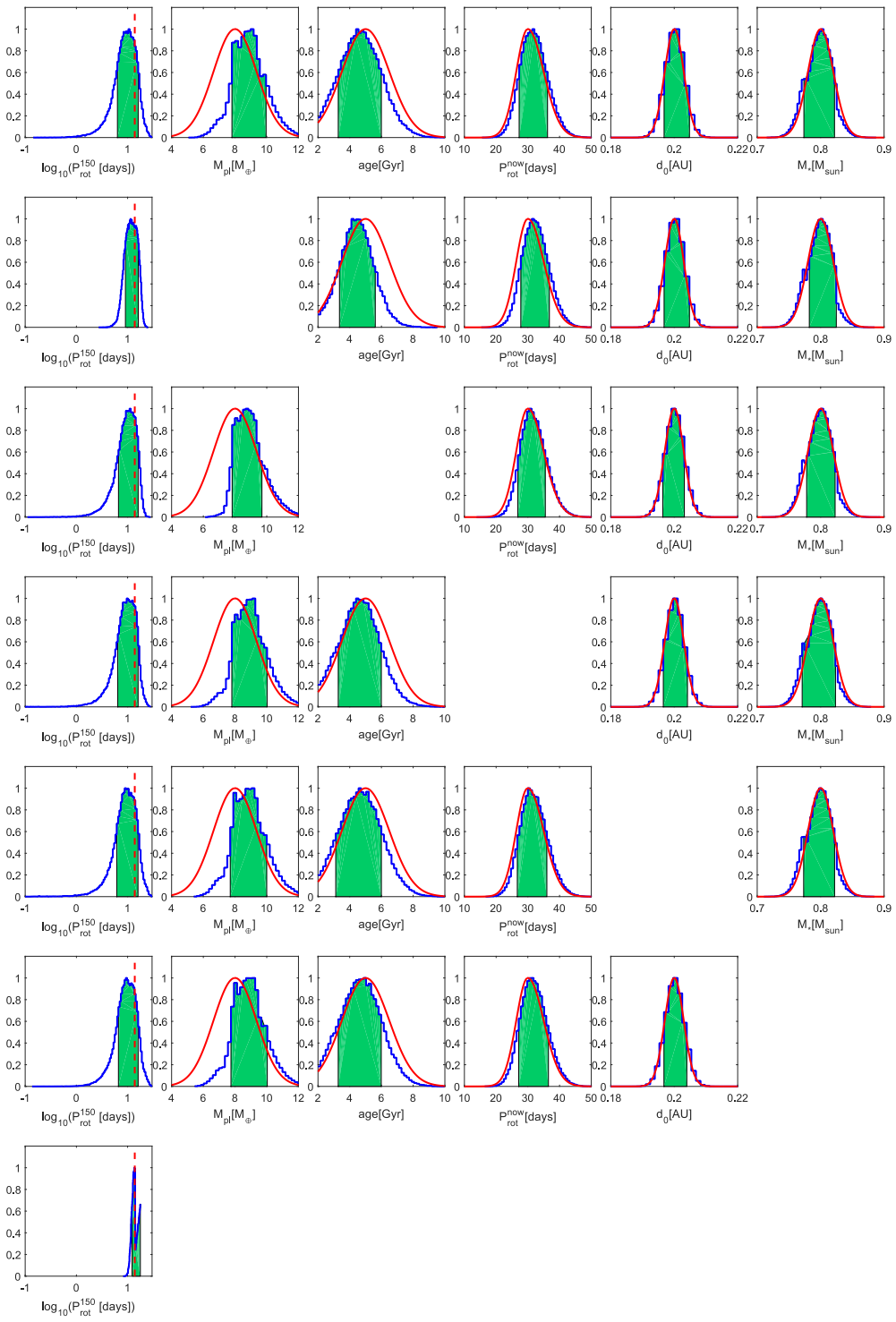

Figure 11. Same as Figure 3, but for the test planet "d" orbiting a slow rotator.

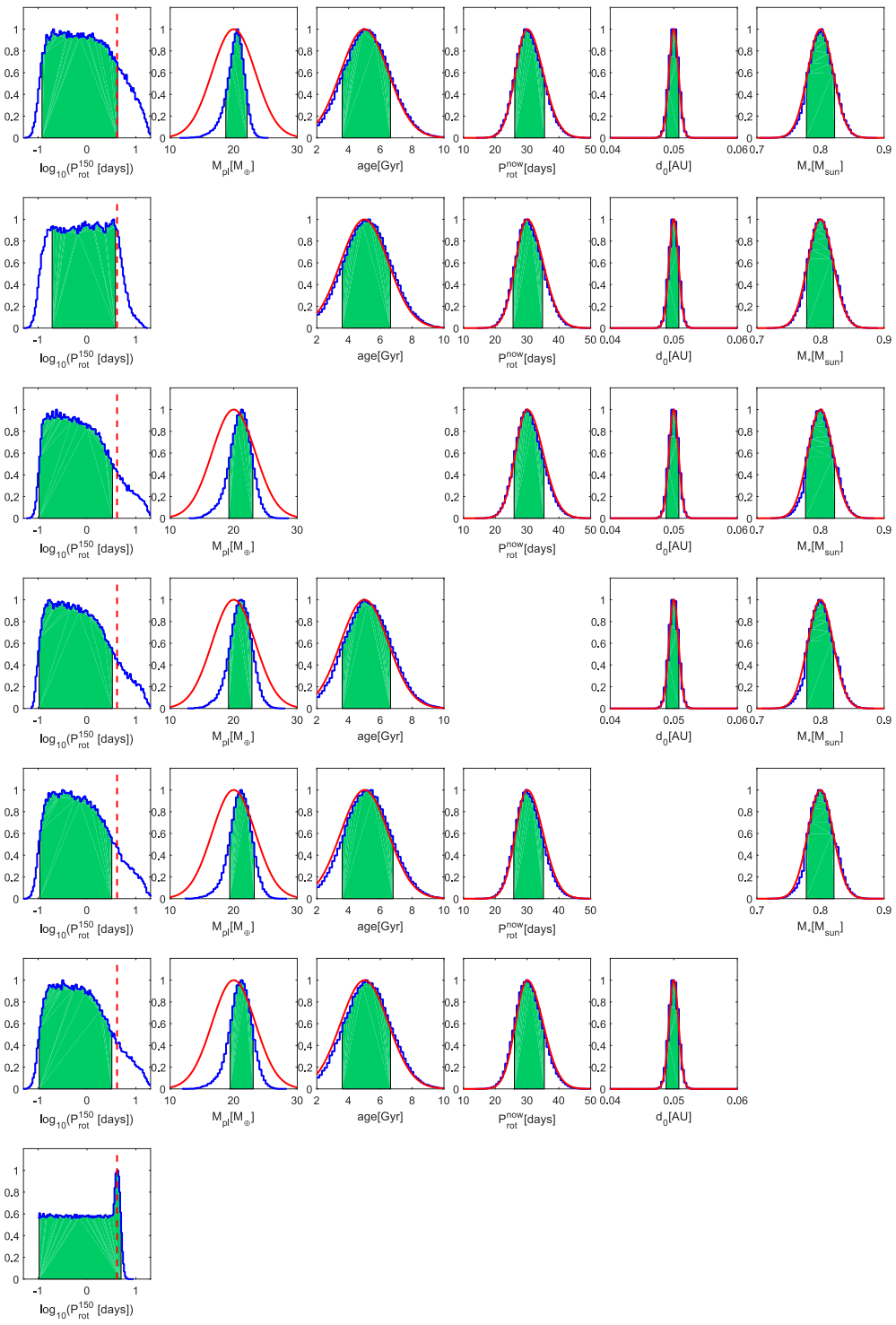

Figure 12. Same as Figure 3, but for the test planet "b" orbiting a medium rotator.

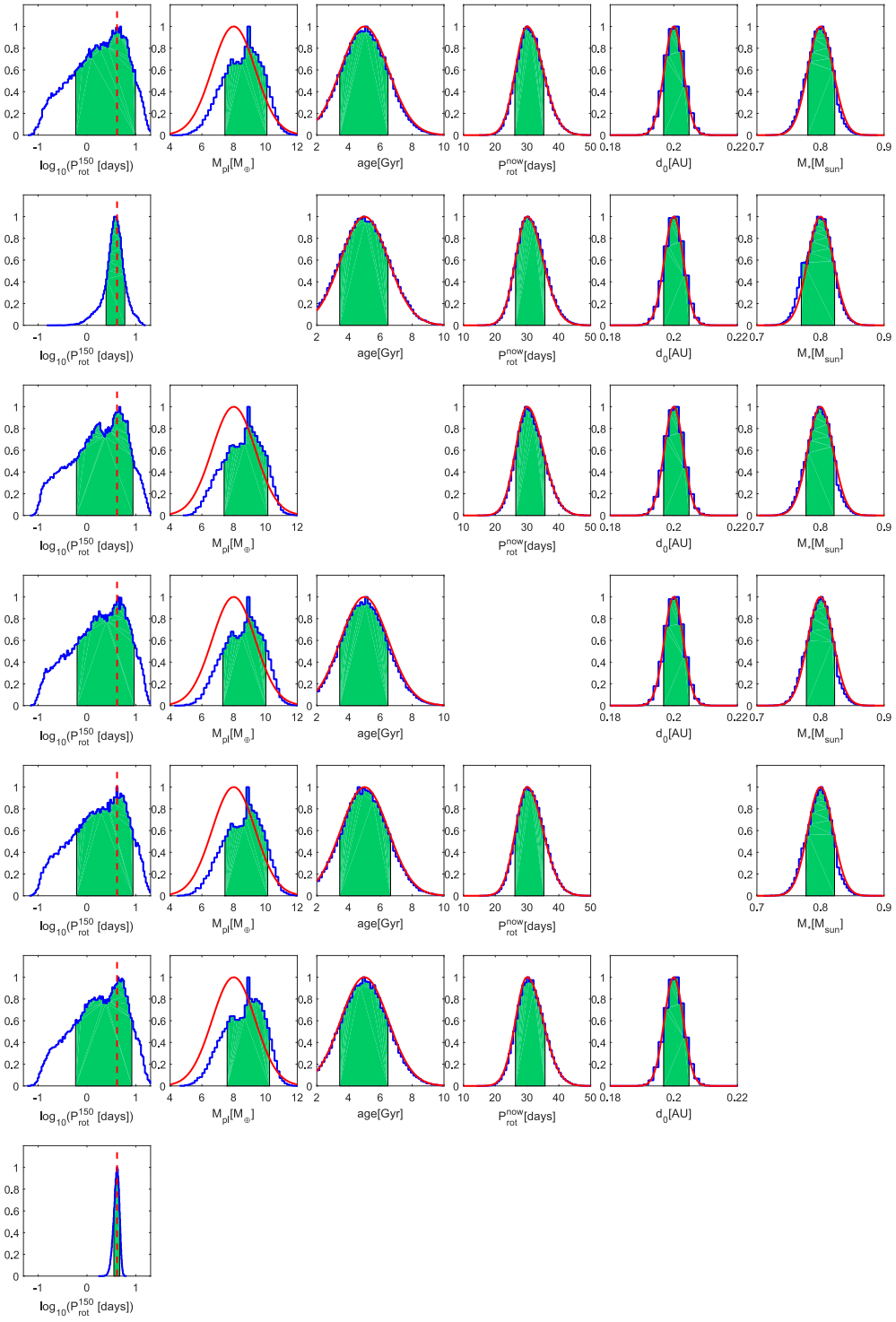

Figure 13. Same as Figure 3, but for the test planet "d" orbiting a medium rotator.

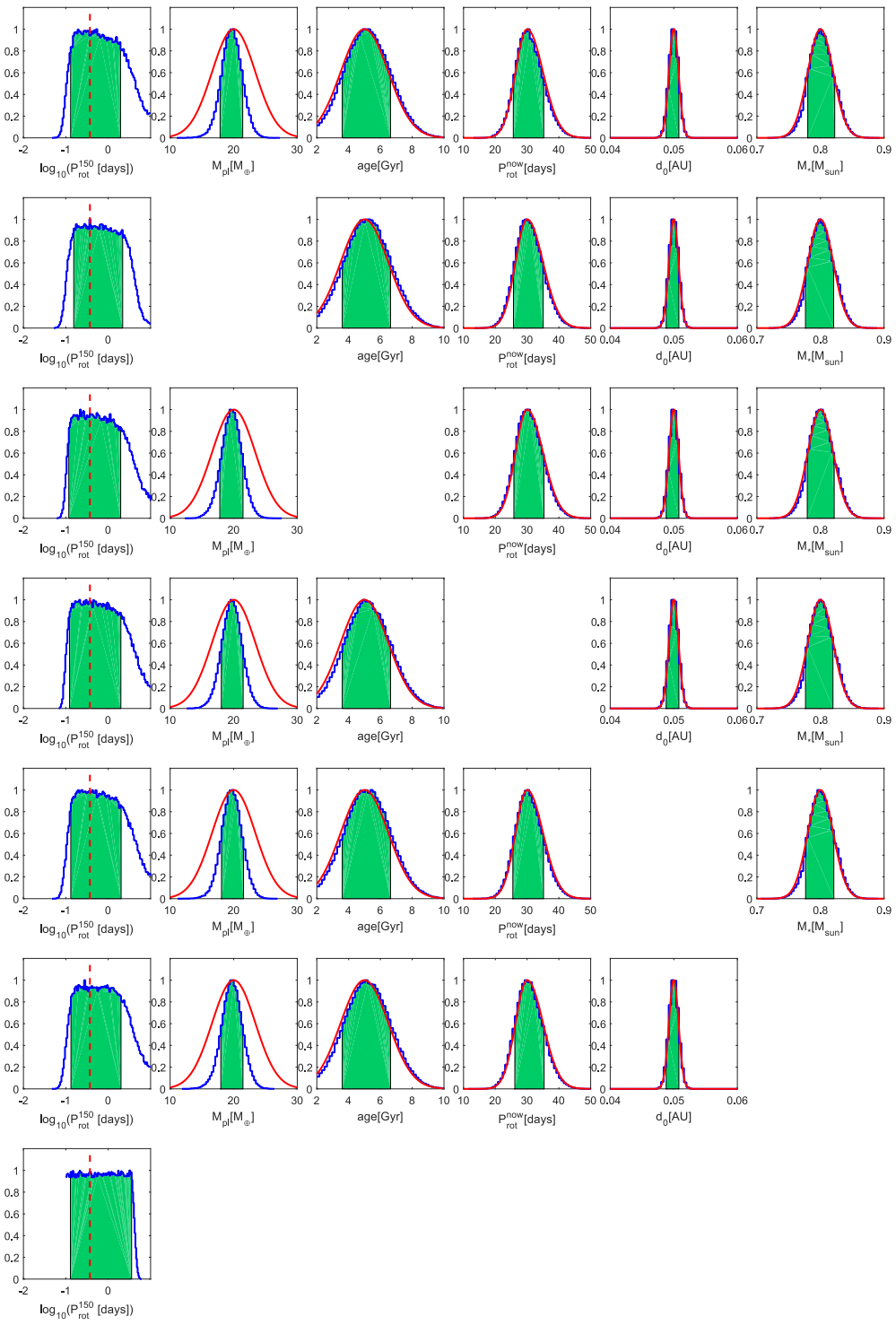

Figure 14. Same as Figure 3, but for the test planet "b" orbiting a fast rotator.

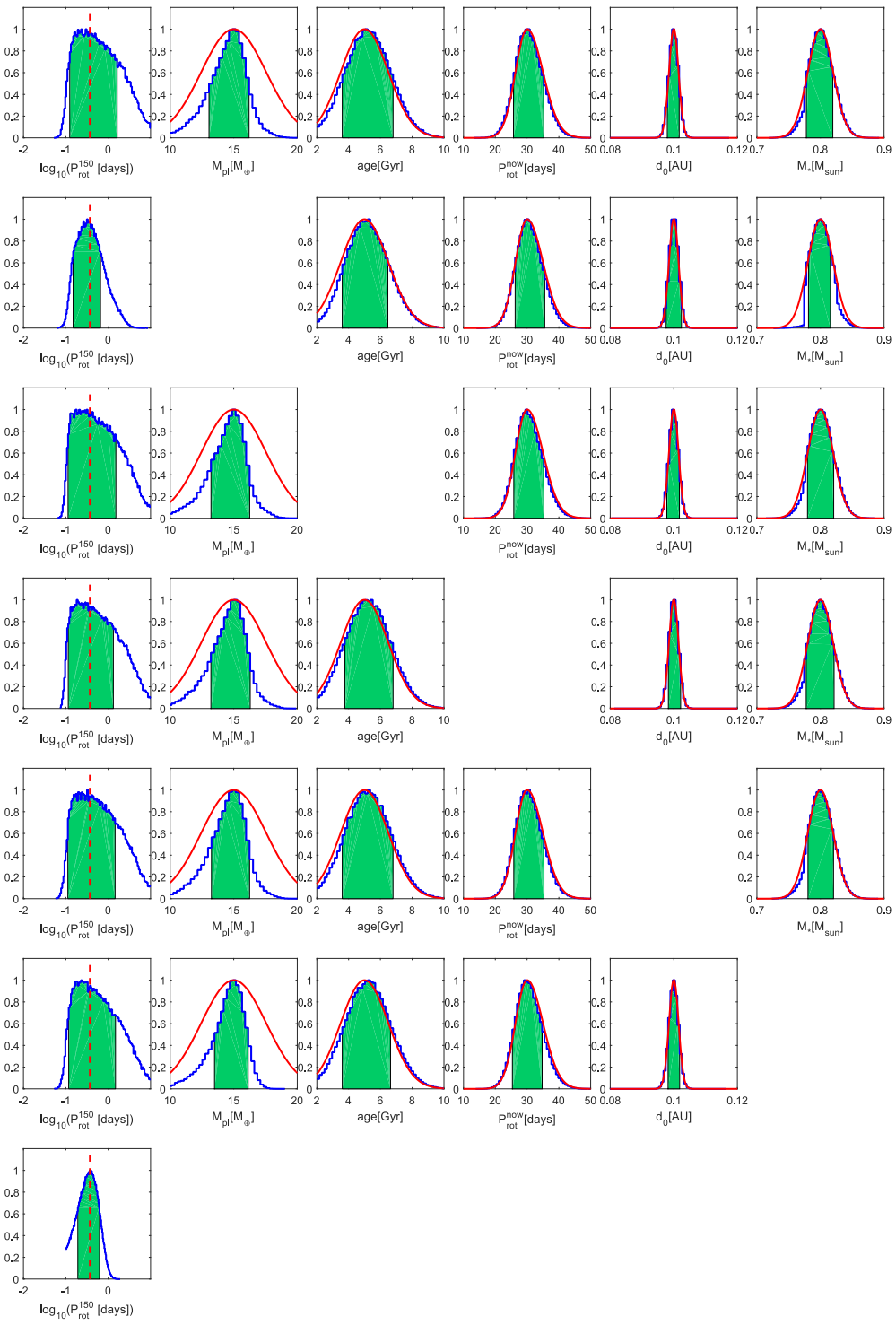

Figure 15. Same as Figure 3, but for the test planet "c" orbiting a fast rotator.

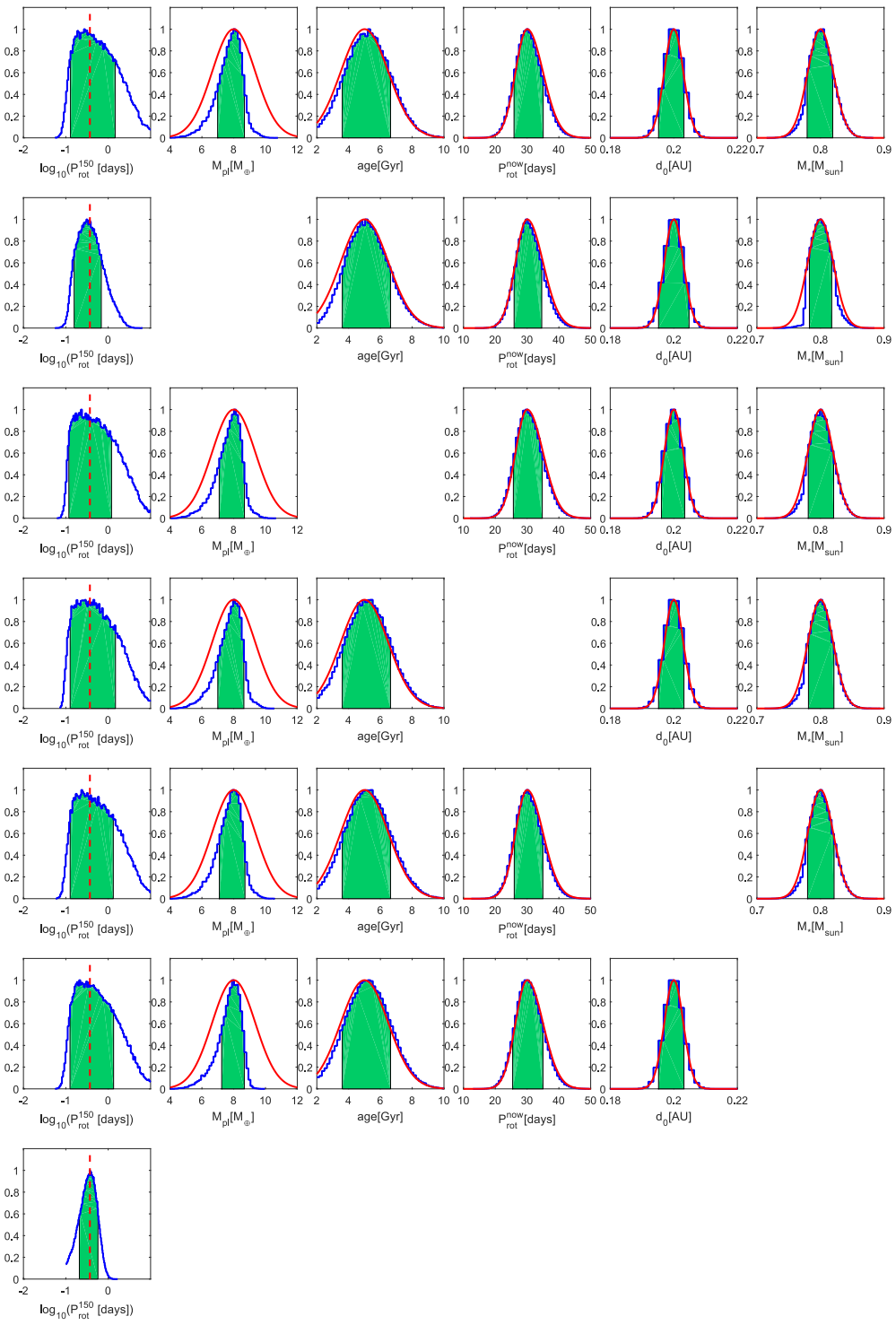

Figure 16. Same as Figure 3, but for the test planet "d" orbiting a fast rotator.

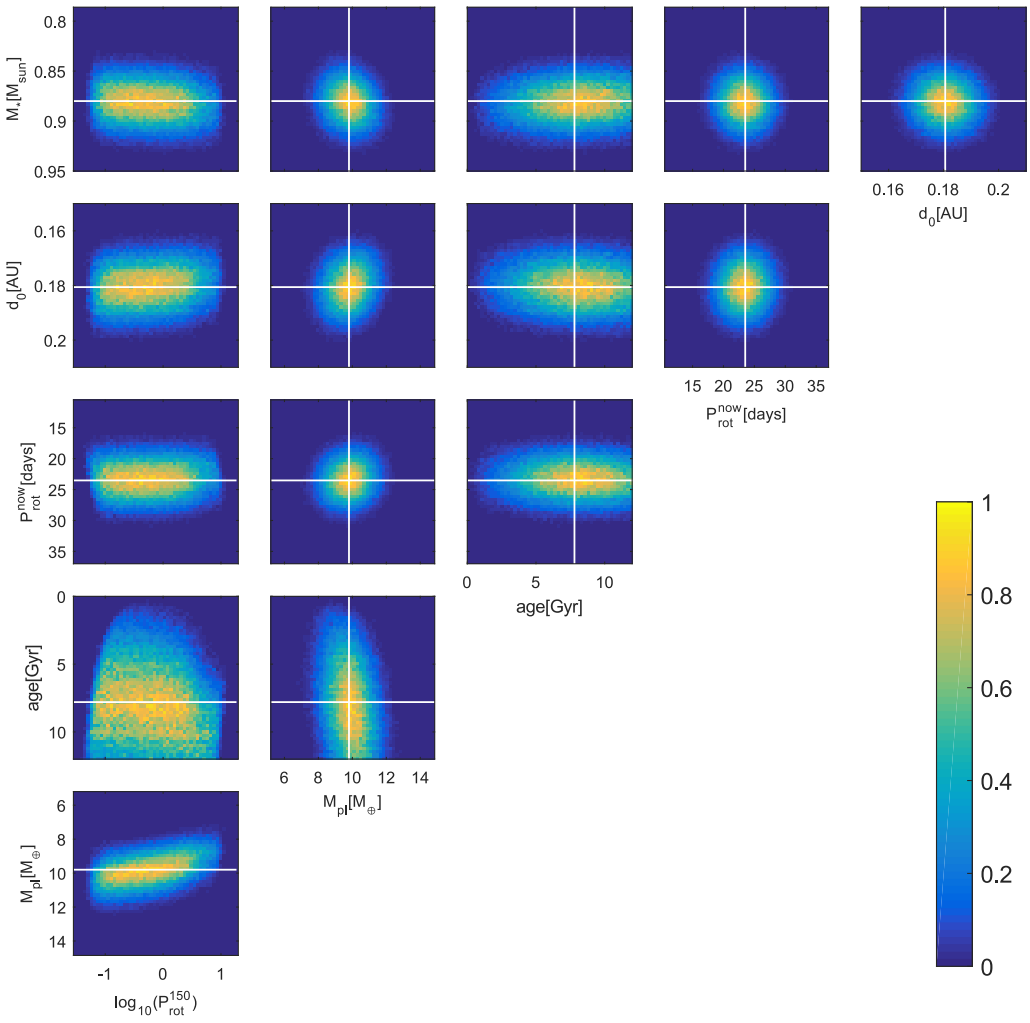

Figure 17. Pair-wise distributions for the parameters involved in the modeling of HD3167c.

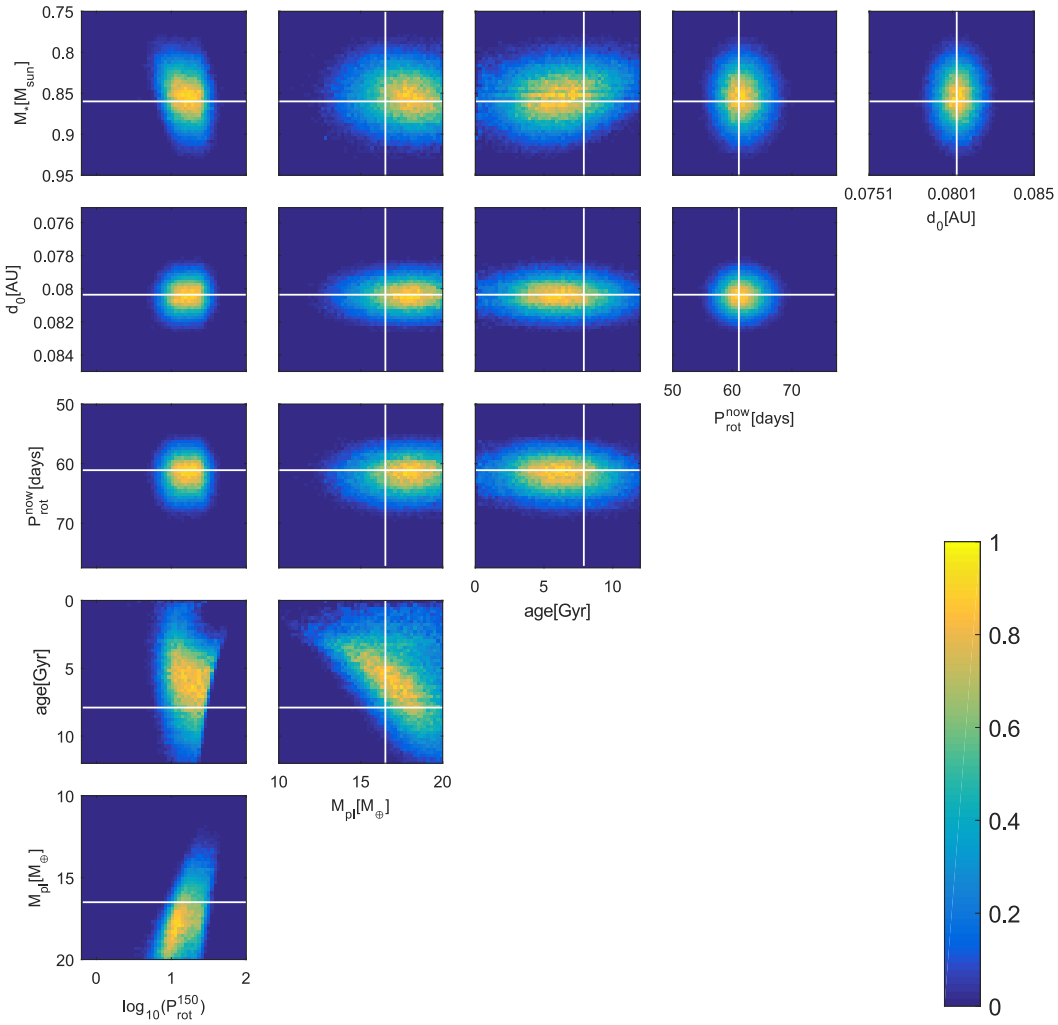

Figure 18. Pair-wise distributions for the parameters involved in the modeling of K2-32b.